Research Article | Vol. 8, No. 3 | 1 Mar 2017 | BIOMEDICAL OPTICS EXPRESS 1823
Biomedical Optics EXPRESS

Embryonic aortic arch hemodynamics are a functional biomarker for ethanol-induced congenital heart defects [Invited]

LINDSY M. PETERSON,[1] SHI GU,[1] GANGA KARUNAMUNI,[2] MICHAEL W. JENKINS,[1,2] MICHIKO WATANABE,[2] AND ANDREW M. ROLLINS[1,*]

[1]*Department of Biomedical Engineering, Case Western Reserve University, Cleveland, Ohio 44106, USA*
[2]*Congenital Heart Collaborative, Rainbow Babies and Children's Hospital, Department of Pediatrics, Case Western Reserve University, Cleveland, Ohio 44106, USA*
[*]*rollins@case.edu*

Abstract: The great arteries develop from symmetrical aortic arch arteries which are extensively remodeled. These events are vulnerable to perturbations. Hemodynamic forces have a significant role in this remodeling. In this study, optical coherence tomography (OCT) visualized live avian embryos for staging and measuring pharyngeal arch morphology. Measurements acquired with our orientation-independent, dual-angle Doppler OCT technique revealed that ethanol exposure leads to higher absolute blood flow, shear stress, and retrograde flow. Ethanol-exposed embryos had smaller cardiac neural crest (CNC) derived pharyngeal arch mesenchyme and fewer migrating CNC-derived cells. These differences in forces and CNC cell numbers could explain the abnormal aortic arch remodeling.

OCIS codes: (110.4500) Optical coherence tomography; (170.3880) Medical and biological imaging.

References and links

1. Centers for Disease Control and Prevention (CDC), "Alcohol use and binge drinking among women of childbearing age--United States, 2006-2010," MMWR Morb. Mortal. Wkly. Rep. **61**(28), 534–538 (2012).
2. L. B. Finer and M. R. Zolna, "Declines in Unintended Pregnancy in the United States, 2008-2011," N. Engl. J. Med. **374**(9), 843–852 (2016).
3. D. S. Walker, C. S. Fisher, A. Sherman, B. Wybrecht, and K. Kyndely, "Fetal alcohol spectrum disorders prevention: an exploratory study of women's use of, attitudes toward, and knowledge about alcohol," J. Am. Acad. Nurse Pract. **17**(5), 187–193 (2005).
4. A. M. Andersen, P. K. Andersen, J. Olsen, M. Grønbæk, and K. Strandberg-Larsen, "Moderate alcohol intake during pregnancy and risk of fetal death," Int. J. Epidemiol. **41**(2), 405–413 (2012).
5. R. Alati, G. Davey Smith, S. J. Lewis, K. Sayal, E. S. Draper, J. Golding, R. Fraser, and R. Gray, "Effect of prenatal alcohol exposure on childhood academic outcomes: contrasting maternal and paternal associations in the ALSPAC study," PLoS One **8**(10), e74844 (2013).
6. B. A. Bailey and R. J. Sokol, "Prenatal alcohol exposure and miscarriage, stillbirth, preterm delivery, and sudden infant death syndrome," Alcohol Res. Health **34**(1), 86–91 (2011).
7. H. S. Feldman, K. L. Jones, S. Lindsay, D. Slymen, H. Klonoff-Cohen, K. Kao, S. Rao, and C. Chambers, "Prenatal alcohol exposure patterns and alcohol-related birth defects and growth deficiencies: a prospective study," Alcohol. Clin. Exp. Res. **36**(4), 670–676 (2012).
8. E. Abel, ed., *Fetal Alcohol syndrome* (Medical Economics Books, Oradell, NJ, 1990).
9. J. Grewal, S. L. Carmichael, C. Ma, E. J. Lammer, and G. M. Shaw, "Maternal periconceptional smoking and alcohol consumption and risk for select congenital anomalies," Birth Defects Res. A Clin. Mol. Teratol. **82**(7), 519–526 (2008).
10. N. D. Harwood H, "Economic implications of the fetal alcohol syndrome," Alcohol Health Res. World **10**, 38–43 (1985).
11. M. L. Kirby and M. R. Hutson, "Factors controlling cardiac neural crest cell migration," Cell Adhes. Migr. **4**(4), 609–621 (2010).
12. T. Hiruma, Y. Nakajima, and H. Nakamura, "Development of pharyngeal arch arteries in early mouse embryo," J. Anat. **201**(1), 15–29 (2002).
13. T. Hiruma and R. Hirakow, "Formation of the pharyngeal arch arteries in the chick embryo. Observations of corrosion casts by scanning electron microscopy," Anat. Embryol. (Berl.) **191**(5), 415–423 (1995).
14. C. S. Le Lièvre and N. M. Le Douarin, "Mesenchymal derivatives of the neural crest: analysis of chimaeric quail and chick embryos," J. Embryol. Exp. Morphol. **34**(1), 125–154 (1975).

#282311 https://doi.org/10.1364/BOE.8.001823
Journal © 2017 Received 7 Dec 2016; revised 27 Jan 2017; accepted 27 Jan 2017; published 24 Feb 2017

Biomedical Optics EXPRESS

15. A. Keyte and M. R. Hutson, "The Neural Crest in Cardiac Congenital Anomalies," Differentiation; Research in Biological Diversity **84**, 25–40 (2012).
16. R. E. Poelmann and A. C. Gittenberger-de Groot, "A subpopulation of apoptosis-prone cardiac neural crest cells targets to the venous pole: multiple functions in heart development?" Dev. Biol. **207**(2), 271–286 (1999).
17. F. A. High, M. Zhang, A. Proweller, L. Tu, M. S. Parmacek, W. S. Pear, and J. A. Epstein, "An essential role for Notch in neural crest during cardiovascular development and smooth muscle differentiation," J. Clin. Invest. **117**(2), 353–363 (2007).
18. A. Nomura-Kitabayashi, C. K. Phoon, S. Kishigami, J. Rosenthal, Y. Yamauchi, K. Abe, K. Yamamura, R. Samtani, C. W. Lo, and Y. Mishina, "Outflow tract cushions perform a critical valve-like function in the early embryonic heart requiring BMPRIA-mediated signaling in cardiac neural crest," Am. J. Physiol. Heart Circ. Physiol. **297**(5), H1617–H1628 (2009).
19. M. R. Hutson and M. L. Kirby, "Model systems for the study of heart development and disease. Cardiac neural crest and conotruncal malformations," Semin. Cell Dev. Biol. **18**(1), 101–110 (2007).
20. T. M. Yelbuz, K. L. Waldo, D. H. Kumiski, H. A. Stadt, R. R. Wolfe, L. Leatherbury, and M. L. Kirby, "Shortened outflow tract leads to altered cardiac looping after neural crest ablation," Circulation **106**(4), 504–510 (2002).
21. K. K. Sulik, M. C. Johnston, and M. A. Webb, "Fetal alcohol syndrome: embryogenesis in a mouse model," Science **214**(4523), 936–938 (1981).
22. L. E. Kotch and K. K. Sulik, "Experimental fetal alcohol syndrome: proposed pathogenic basis for a variety of associated facial and brain anomalies," Am. J. Med. Genet. **44**(2), 168–176 (1992).
23. M. M. Cartwright and S. M. Smith, "Increased cell death and reduced neural crest cell numbers in ethanol-exposed embryos: partial basis for the fetal alcohol syndrome phenotype," Alcohol. Clin. Exp. Res. **19**(2), 378–386 (1995).
24. M. M. Cartwright, L. L. Tessmer, and S. M. Smith, "Ethanol-induced neural crest apoptosis is coincident with their endogenous death, but is mechanistically distinct," Alcohol. Clin. Exp. Res. **22**(1), 142–149 (1998).
25. R. A. Rovasio and N. L. Battiato, "Ethanol induces morphological and dynamic changes on in vivo and in vitro neural crest cells," Alcohol. Clin. Exp. Res. **26**(8), 1286–1298 (2002).
26. J. Czarnobaj, K. M. Bagnall, J. S. Bamforth, and N. C. Milos, "The different effects on cranial and trunk neural crest cell behaviour following exposure to a low concentration of alcohol in vitro," Arch. Oral Biol. **59**(5), 500–512 (2014).
27. B. Hogers, M. C. DeRuiter, A. C. Gittenberger-de Groot, and R. E. Poelmann, "Extraembryonic venous obstructions lead to cardiovascular malformations and can be embryolethal," Cardiovasc. Res. **41**(1), 87–99 (1999).
28. B. Hogers, M. C. DeRuiter, A. C. Gittenberger-de Groot, and R. E. Poelmann, "Unilateral Vitelline Vein Ligation Alters Intracardiac Blood Flow Patterns and Morphogenesis in the Chick Embryo," Circ. Res. **80**(4), 473–481 (1997).
29. N. Hu, D. A. Christensen, A. K. Agrawal, C. Beaumont, E. B. Clark, and J. A. Hawkins, "Dependence of Aortic Arch Morphogenesis on Intracardiac Blood Flow in the Left Atrial Ligated Chick Embryo," Anat. Rec. (Hoboken) **292**(5), 652–660 (2009).
30. S. Gu, M. W. Jenkins, L. M. Peterson, Y.-Q. Doughman, A. M. Rollins, and M. Watanabe, "Optical Coherence Tomography Captures Rapid Hemodynamic Responses to Acute Hypoxia in the Cardiovascular System of Early Embryos," Dev. Dyn. **241**(3), 534–544 (2012).
31. G. Karunamuni, S. Gu, Y. Q. Doughman, L. M. Peterson, K. Mai, Q. McHale, M. W. Jenkins, K. K. Linask, A. M. Rollins, and M. Watanabe, "Ethanol exposure alters early cardiac function in the looping heart: a mechanism for congenital heart defects?" Am. J. Physiol. Heart Circ. Physiol. **306**(3), H414–H421 (2014).
32. L. M. Peterson, S. Gu, M. W. Jenkins, and A. M. Rollins, "Orientation-independent rapid pulsatile flow measurement using dual-angle Doppler OCT," Biomed. Opt. Express **5**(2), 499–514 (2014).
33. G. Karunamuni, S. Gu, Y. Q. Doughman, A. I. Noonan, A. M. Rollins, M. W. Jenkins, and M. Watanabe, "Using optical coherence tomography to rapidly phenotype and quantify congenital heart defects associated with prenatal alcohol exposure," Dev. Dyn. **244**(4), 607–618 (2015).
34. P. Vennemann, K. T. Kiger, R. Lindken, B. C. Groenendijk, S. Stekelenburg-de Vos, T. L. ten Hagen, N. T. Ursem, R. E. Poelmann, J. Westerweel, and B. P. Hierck, "In vivo micro particle image velocimetry measurements of blood-plasma in the embryonic avian heart," J. Biomech. **39**(7), 1191–1200 (2006).
35. Y. Wang, O. Dur, M. J. Patrick, J. P. Tinney, K. Tobita, B. B. Keller, and K. Pekkan, "Aortic arch morphogenesis and flow modeling in the chick embryo," Ann. Biomed. Eng. **37**(6), 1069–1081 (2009).
36. W. J. Kowalski, O. Dur, Y. Wang, M. J. Patrick, J. P. Tinney, B. B. Keller, and K. Pekkan, "Critical transitions in early embryonic aortic arch patterning and hemodynamics," PLoS One **8**(3), e60271 (2013).
37. D. Huang, E. A. Swanson, C. P. Lin, J. S. Schuman, W. G. Stinson, W. Chang, M. R. Hee, T. Flotte, K. Gregory, C. A. Puliafito, and et, "Optical coherence tomography," Science **254**(5035), 1178–1181 (1991).
38. S. Marschall, B. Sander, M. Mogensen, T. M. Jørgensen, and P. E. Andersen, "Optical coherence tomography-current technology and applications in clinical and biomedical research," Anal. Bioanal. Chem. **400**(9), 2699–2720 (2011).
39. R. Raghunathan, M. Singh, M. E. Dickinson, and K. V. Larin, "Optical coherence tomography for embryonic imaging: a review," J. Biomed. Opt. **21**(5), 050902 (2016).

Biomedical Optics EXPRESS

40. J. Men, Y. Huang, J. Solanki, X. Zeng, A. Alex, J. Jerwick, Z. Zhang, R. E. Tanzi, A. Li, and C. Zhou, "Optical Coherence Tomography for Brain Imaging and Developmental Biology," IEEE J. Sel. Top. Quantum Electron. **22**(4), 120–132 (2016).
41. S. A. Boppart, M. E. Brezinski, B. E. Bouma, G. J. Tearney, and J. G. Fujimoto, "Investigation of Developing Embryonic Morphology using Optical Coherence Tomography," Dev. Biol. **177**(1), 54–63 (1996).
42. S. A. Boppart, G. J. Tearney, B. E. Bouma, J. F. Southern, M. E. Brezinski, and J. G. Fujimoto, "Noninvasive assessment of the developing Xenopus cardiovascular system using optical coherence tomography," Proc. Natl. Acad. Sci. U.S.A. **94**(9), 4256–4261 (1997).
43. I. V. Larina, E. F. Carbajal, V. V. Tuchin, M. E. Dickinson, and K. V. Larin, "Enhanced OCT imaging of embryonic tissue with optical clearing," Laser Phys. Lett. **5**(6), 476–479 (2008).
44. I. V. Larina, S. Ivers, S. Syed, M. E. Dickinson, and K. V. Larin, "Hemodynamic measurements from individual blood cells in early mammalian embryos with Doppler swept source OCT," Opt. Lett. **34**(7), 986–988 (2009).
45. M. W. Jenkins, F. Rothenberg, D. Roy, V. P. Nikolski, Z. Hu, M. Watanabe, D. L. Wilson, I. R. Efimov, and A. M. Rollins, "4D embryonic cardiography using gated optical coherence tomography," Opt. Express **14**(2), 736–748 (2006).
46. W. Luo, D. L. Marks, T. S. Ralston, and S. A. Boppart, "Three-dimensional optical coherence tomography of the embryonic murine cardiovascular system," J. Biomed. Opt. **11**(2), 021014 (2006).
47. M. W. Jenkins, P. Patel, H. Deng, M. M. Montano, M. Watanabe, and A. M. Rollins, "Phenotyping transgenic embryonic murine hearts using optical coherence tomography," Appl. Opt. **46**(10), 1776–1781 (2007).
48. S. Yazdanfar, M. Kulkarni, and J. Izatt, "High resolution imaging of in vivo cardiac dynamics using color Doppler optical coherence tomography," Opt. Express **1**(13), 424–431 (1997).
49. V. X. D. Yang, M. Gordon, E. Seng-Yue, S. Lo, B. Qi, J. Pekar, A. Mok, B. Wilson, and I. Vitkin, "High speed, wide velocity dynamic range Doppler optical coherence tomography (Part II): Imaging in vivo cardiac dynamics of Xenopus laevis," Opt. Express **11**(14), 1650–1658 (2003).
50. A. Mariampillai, B. A. Standish, N. R. Munce, C. Randall, G. Liu, J. Y. Jiang, A. E. Cable, I. A. Vitkin, and V. X. D. Yang, "Doppler optical cardiogram gated 2D color flow imaging at 1000 fps and 4D in vivo visualization of embryonic heart at 45 fps on a swept source OCT system," Opt. Express **15**(4), 1627–1638 (2007).
51. R. Yelin, D. Yelin, W.-Y. Oh, S. H. Yun, C. Boudoux, B. J. Vakoc, B. E. Bouma, and G. J. Tearney, "Multimodality optical imaging of embryonic heart microstructure," J. Biomed. Opt. **12**(6), 064021 (2007).
52. A. Bradu, L. Ma, J. W. Bloor, and A. Podoleanu, "Dual optical coherence tomography/fluorescence microscopy for monitoring of Drosophila melanogaster larval heart," J. Biophotonics **2**(6-7), 380–388 (2009).
53. M. A. Choma, S. D. Izatt, R. J. Wessells, R. Bodmer, and J. A. Izatt, "Images in cardiovascular medicine: in vivo imaging of the adult Drosophila melanogaster heart with real-time optical coherence tomography," Circulation **114**(2), e35–e36 (2006).
54. N. V. Iftimia, D. X. Hammer, R. D. Ferguson, M. Mujat, D. Vu, and A. A. Ferrante, "Dual-beam Fourier domain optical Doppler tomography of zebrafish," Opt. Express **16**(18), 13624–13636 (2008).
55. L. Kagemann, H. Ishikawa, J. Zou, P. Charukamnoetkanok, G. Wollstein, K. A. Townsend, M. L. Gabriele, N. Bahary, X. Wei, J. G. Fujimoto, and J. S. Schuman, "Repeated, noninvasive, high resolution spectral domain optical coherence tomography imaging of zebrafish embryos," Mol. Vis. **14**, 2157–2170 (2008).
56. B. Garita, M. W. Jenkins, M. Han, C. Zhou, M. Vanauker, A. M. Rollins, M. Watanabe, J. G. Fujimoto, and K. K. Linask, "Blood flow dynamics of one cardiac cycle and relationship to mechanotransduction and trabeculation during heart looping," Am. J. Physiol. Heart Circ. Physiol. **300**(3), H879–H891 (2011).
57. S. Gu, M. W. Jenkins, M. Watanabe, and A. M. Rollins, "Optical Coherence Tomography Imaging of Early Quail Embryos," Cold Spring Harbor Protocols **2011**, pdb.prot5564 (2011).
58. M. Gargesha, M. W. Jenkins, D. L. Wilson, and A. M. Rollins, "High temporal resolution OCT using image-based retrospective gating," Opt. Express **17**(13), 10786–10799 (2009).
59. L. M. Peterson, M. W. Jenkins, S. Gu, L. Barwick, M. Watanabe, and A. M. Rollins, "4D shear stress maps of the developing heart using Doppler optical coherence tomography," Biomed. Opt. Express **3**(11), 3022–3032 (2012).
60. T. M. Yelbuz, M. A. Choma, L. Thrane, M. L. Kirby, and J. A. Izatt, "Optical Coherence Tomography A New High-Resolution Imaging Technology to Study Cardiac Development in Chick Embryos," Circulation **106**, 2771–2774 (2002).
61. B. A. Filas, I. R. Efimov, and L. A. Taber, "Optical coherence tomography as a tool for measuring morphogenetic deformation of the looping heart," Anat. Rec. (Hoboken) **290**(9), 1057–1068 (2007).
62. A. M. Davis, F. G. Rothenberg, N. Shepherd, and J. A. Izatt, "In vivo spectral domain optical coherence tomography volumetric imaging and spectral Doppler velocimetry of early stage embryonic chicken heart development," J. Opt. Soc. Am. A **25**(12), 3134–3143 (2008).
63. L. Thrane, H. E. Larsen, K. Norozi, F. Pedersen, J. B. Thomsen, M. Trojer, and T. M. Yelbuz, "Field programmable gate-array-based real-time optical Doppler tomography system for in vivo imaging of cardiac dynamics in the chick embryo," Optice **48**, 023201 (2009).
64. A. Ramasubramanian, N. L. Nerurkar, K. H. Achtien, B. A. Filas, D. A. Voronov, and L. A. Taber, "On Modeling Morphogenesis of the Looping Heart Following Mechanical Perturbations," J. Biomech. Eng. **130**(6), 061018 (2008).

Biomedical Optics EXPRESS

65. Z. Ma and X. Tao, "Two wavelength spectral domain optical coherence tomography systems for early stage chicken embryonic heart imaging," in *2012 IEEE International Conference on Virtual Environments Human-Computer Interfaces and Measurement Systems (VECIMS) Proceedings*, 2012), 13–16.
66. A. Liu, X. Yin, L. Shi, P. Li, K. L. Thornburg, R. Wang, and S. Rugonyi, "Biomechanics of the chick embryonic heart outflow tract at HH18 using 4D optical coherence tomography imaging and computational modeling," PLoS One **7**(7), e40869 (2012).
67. W. J. Kowalski, N. C. Teslovich, C.-Y. Chen, B. B. Keller, and K. Pekkan, "Simultaneous real-time quantification of blood flow and vascular growth in the chick embryo using optical coherence tomography," Proc. SPIE **8953**, 895307 (2014).
68. P. Li, A. Liu, L. Shi, X. Yin, S. Rugonyi, and R. K. Wang, "Assessment of strain and strain rate in embryonic chick heart in vivo using tissue Doppler optical coherence tomography," Phys. Med. Biol. **56**(22), 7081–7092 (2011).
69. S. Bhat, I. V. Larina, K. V. Larin, M. E. Dickinson, and M. Liebling, "4D reconstruction of the beating embryonic heart from two orthogonal sets of parallel optical coherence tomography slice-sequences," IEEE Trans. Med. Imaging **32**(3), 578–588 (2013).
70. S. Wang, D. S. Lakomy, M. D. Garcia, A. L. Lopez 3rd, K. V. Larin, and I. V. Larina, "Four-dimensional live imaging of hemodynamics in mammalian embryonic heart with Doppler optical coherence tomography," J. Biophotonics **9**(8), 837–847 (2016).
71. S. Wang, M. Singh, A. L. Lopez 3rd, C. Wu, R. Raghunathan, A. Schill, J. Li, K. V. Larin, and I. V. Larina, "Direct four-dimensional structural and functional imaging of cardiovascular dynamics in mouse embryos with 1.5 MHz optical coherence tomography," Opt. Lett. **40**(20), 4791–4794 (2015).
72. Z. Ma, S. Dou, Y. Zhao, C. Guo, J. Liu, Q. Wang, T. Xu, R. K. Wang, and Y. Wang, "In vivo assessment of wall strain in embryonic chick heart by spectral domain optical coherence tomography," Appl. Opt. **54**(31), 9253–9257 (2015).
73. P. Li, X. Yin, L. Shi, S. Rugonyi, and R. K. Wang, "In vivo functional imaging of blood flow and wall strain rate in outflow tract of embryonic chick heart using ultrafast spectral domain optical coherence tomography," J. Biomed. Opt. **17**(9), 096006 (2012).
74. A. Davis, J. Izatt, and F. Rothenberg, "Quantitative Measurement of Blood Flow Dynamics in Embryonic Vasculature Using Spectral Doppler Velocimetry," Anat. Rec. (Hoboken) **292**(3), 311–319 (2009).
75. P. Li, A. Liu, L. Shi, X. Yin, S. Rugonyi, and R. K. Wang, "Assessment of strain and strain rate in embryonic chick heart in vivo using tissue Doppler optical coherence tomography," Phys. Med. Biol. **56**(22), 7081–7092 (2011).
76. Z. Ma, A. Liu, X. Yin, A. Troyer, K. Thornburg, R. K. Wang, and S. Rugonyi, "Measurement of absolute blood flow velocity in outflow tract of HH18 chicken embryo based on 4D reconstruction using spectral domain optical coherence tomography," Biomed. Opt. Express **1**(3), 798–811 (2010).
77. T. G. van Leeuwen, M. D. Kulkarni, S. Yazdanfar, A. M. Rollins, and J. A. Izatt, "High-flow-velocity and shear-rate imaging by use of color Doppler optical coherence tomography," Opt. Lett. **24**(22), 1584–1586 (1999).
78. S. Rugonyi, C. Shaut, A. Liu, K. Thornburg, and R. K. Wang, "Changes in wall motion and blood flow in the outflow tract of chick embryonic hearts observed with optical coherence tomography after outflow tract banding and vitelline-vein ligation," Phys. Med. Biol. **53**(18), 5077–5091 (2008).
79. V. K. Chivukula, S. Goenezen, A. Liu, and S. Rugonyi, "Effect of Outflow Tract Banding on Embryonic Cardiac Hemodynamics," J. Cardiovasc. Dev. Dis. **3**(1), 1 (2015).
80. L. M. Peterson, M. McPheeters, L. Barwick, S. Gu, A. M. Rollins, and M. W. Jenkins, "Altering embryonic cardiac dynamics with optical pacing," in *2012 Annual International Conference of the IEEE Engineering in Medicine and Biology Society*, 2012), 1382–1385.
81. R. Michaely, A. H. Bachmann, M. L. Villiger, C. Blatter, T. Lasser, and R. A. Leitgeb, "Vectorial reconstruction of retinal blood flow in three dimensions measured with high resolution resonant Doppler Fourier domain optical coherence tomography," J. Biomed. Opt. **12**(4), 041213 (2007).
82. S. Makita, T. Fabritius, and Y. Yasuno, "Quantitative retinal-blood flow measurement with three-dimensional vessel geometry determination using ultrahigh-resolution Doppler optical coherence angiography," Opt. Lett. **33**(8), 836–838 (2008).
83. D. P. Davé and T. E. Milner, "Doppler-angle measurement in highly scattering media," Opt. Lett. **25**(20), 1523–1525 (2000).
84. C. J. Pedersen, D. Huang, M. A. Shure, and A. M. Rollins, "Measurement of absolute flow velocity vector using dual-angle, delay-encoded Doppler optical coherence tomography," Opt. Lett. **32**(5), 506–508 (2007).
85. Y.-C. Ahn, W. Jung, and Z. Chen, "Quantification of a three-dimensional velocity vector using spectral-domain Doppler optical coherence tomography," Opt. Lett. **32**(11), 1587–1589 (2007).
86. N. V. Iftimia, D. X. Hammer, R. D. Ferguson, M. Mujat, D. Vu, and A. A. Ferrante, "Dual-beam Fourier domain optical Doppler tomography of zebrafish," Opt. Express **16**(18), 13624–13636 (2008).
87. R. M. Werkmeister, N. Dragostinoff, M. Pircher, E. Götzinger, C. K. Hitzenberger, R. A. Leitgeb, and L. Schmetterer, "Bidirectional Doppler Fourier-domain optical coherence tomography for measurement of absolute flow velocities in human retinal vessels," Opt. Lett. **33**(24), 2967–2969 (2008).
88. C. Blatter, S. Coquoz, B. Grajciar, A. S. G. Singh, M. Bonesi, R. M. Werkmeister, L. Schmetterer, and R. A. Leitgeb, "Dove prism based rotating dual beam bidirectional Doppler OCT," Biomed. Opt. Express **4**(7), 1188–1203 (2013).

Biomedical Optics EXPRESS

89. M. Serrano, M. Han, P. Brinez, and K. K. Linask, "Fetal alcohol syndrome: cardiac birth defects in mice and prevention with folate," Am. J. Obstet. Gynecol. **203**(1), 75.e7 (2010).
90. M. W. Jenkins, M. Watanabe, and A. M. Rollins, "Longitudinal Imaging of Heart Development With Optical Coherence Tomography," IEEE J. Sel. Top. Quantum Electron. **18**(3), 1166–1175 (2012).
91. Z. Hu and A. Rollins, "Quasi-telecentric optical design of a microscope-compatible OCT scanner," Opt. Express **13**(17), 6407–6415 (2005).
92. V. Hamburger and H. L. Hamilton, "A series of normal stages in the development of the chick embryo," J. Morphol. **88**(1), 49–92 (1951).
93. S. J. Ainsworth, R. L. Stanley, and D. J. R. Evans, "Developmental stages of the Japanese quail," J. Anat. **216**(1), 3–15 (2010).
94. M. W. Jenkins, L. Peterson, S. Gu, M. Gargesha, D. L. Wilson, M. Watanabe, and A. M. Rollins, "Measuring hemodynamics in the developing heart tube with four-dimensional gated Doppler optical coherence tomography," J. Biomed. Opt. **15**(6), 066022 (2010).
95. C. A. Taylor, T. J. R. Hughes, and C. K. Zarins, "Finite element modeling of three-dimensional pulsatile flow in the abdominal aorta: relevance to atherosclerosis," Ann. Biomed. Eng. **26**(6), 975–987 (1998).
96. J. Vermot, A. S. Forouhar, M. Liebling, D. Wu, D. Plummer, M. Gharib, and S. E. Fraser, "Reversing Blood Flows Act Through *klf2a* to Ensure Normal Valvulogenesis in the Developing Heart," PLoS Biol. **7**(11), e1000246 (2009).
97. S. M. Ford, M. T. McPheeters, Y. T. Wang, S. Gu, Y. Q. Doughman, J. P. Strainic, C. S. Snyder, A. M. Rollins, M. Watanabe, and M. W. Jenkins, "Increased regurgitant flow causes endocardial cushion defects in an avian embryonic model of congenital heart disease," accepted.
98. P. A. Trainor and P. P. Tam, "Cranial paraxial mesoderm and neural crest cells of the mouse embryo: co-distribution in the craniofacial mesenchyme but distinct segregation in branchial arches," Development **121**(8), 2569–2582 (1995).
99. M. Bergwerff, M. E. Verberne, M. C. DeRuiter, R. E. Poelmann, and A. C. Gittenberger-de Groot, "Neural Crest Cell Contribution to the Developing Circulatory System: Implications for Vascular Morphology?" Circ. Res. **82**(2), 221–231 (1998).
100. S. Miyagawa-Tomita, K. Waldo, H. Tomita, and M. L. Kirby, "Temporospatial study of the migration and distribution of cardiac neural crest in quail-chick chimeras," Am. J. Anat. **192**(1), 79–88 (1991).
101. K. L. Waldo and M. L. Kirby, "Cardiac neural crest contribution to the pulmonary artery and sixth aortic arch artery complex in chick embryos aged 6 to 18 days," Anat. Rec. **237**(3), 385–399 (1993).
102. E. Goldmuntz, D. A. Driscoll, B. S. Emanuel, D. McDonald-McGinn, M. Mei, E. Zackai, and L. E. Mitchell, "Evaluation of potential modifiers of the cardiac phenotype in the 22q11.2 deletion syndrome," Birth Defects Res. A Clin. Mol. Teratol. **85**(2), 125–129 (2009).
103. G. H. Karunamuni, P. Ma, S. Gu, A. M. Rollins, M. W. Jenkins, and M. Watanabe, "Connecting teratogen-induced congenital heart defects to neural crest cells and their effect on cardiac function," Birth Defects Res. C Embryo Today **102**(3), 227–250 (2014).
104. K. Boric, P. Orio, T. Viéville, and K. Whitlock, "Quantitative Analysis of Cell Migration Using Optical Flow," PLoS One **8**(7), e69574 (2013).
105. C. P. Klingenberg, L. Wetherill, J. Rogers, E. Moore, R. Ward, I. Autti-Rämö, A. Fagerlund, S. W. Jacobson, L. K. Robinson, H. E. Hoyme, S. N. Mattson, T. K. Li, E. P. Riley, and T. Foroud; CIFASD Consortium, "Prenatal alcohol exposure alters the patterns of facial asymmetry," Alcohol **44**(7-8), 649–657 (2010).
106. D. E. Stewart, M. L. Kirby, and K. K. Sulik, "Hemodynamic changes in chick embryos precede heart defects after cardiac neural crest ablation," Circ. Res. **59**(5), 545–550 (1986).
107. L. Leatherbury, D. S. Braden, H. Tomita, H. E. Gauldin, and W. F. Jackson, "Hemodynamic changes. Wall stresses and pressure gradients in neural crest-ablated chick embryos," Ann. N. Y. Acad. Sci. **588**(1 Embryonic Ori), 305–313 (1990).
108. L. Leatherbury, D. M. Connuck, H. E. Gauldin, and M. L. Kirby, "Hemodynamic changes and compensatory mechanisms during early cardiogenesis after neural crest ablation in chick embryos," Pediatr. Res. **30**(6), 509–512 (1991).
109. H. Tomita, D. M. Connuck, L. Leatherbury, and M. L. Kirby, "Relation of early hemodynamic changes to final cardiac phenotype and survival after neural crest ablation in chick embryos," Circulation **84**(3), 1289–1295 (1991).
110. M. J. Farrell, J. L. Burch, K. Wallis, L. Rowley, D. Kumiski, H. Stadt, R. E. Godt, T. L. Creazzo, and M. L. Kirby, "FGF-8 in the ventral pharynx alters development of myocardial calcium transients after neural crest ablation," J. Clin. Invest. **107**(12), 1509–1517 (2001).
111. K. Waldo, M. Zdanowicz, J. Burch, D. H. Kumiski, H. A. Stadt, R. E. Godt, T. L. Creazzo, and M. L. Kirby, "A novel role for cardiac neural crest in heart development," J. Clin. Invest. **103**(11), 1499–1507 (1999).
112. P. Ma, S. Gu, G. H. Karunamuni, M. W. Jenkins, M. Watanabe, and A. M. Rollins, "Cardiac neural crest ablation results in early endocardial cushion and hemodynamic flow abnormalities," Am. J. Physiol. Heart Circ. Physiol. **311**(5), H1150–H1159 (2016).

Biomedical Optics EXPRESS

1. Introduction

A recent survey of 345,076 women aged 18-44 years in the United States found that 7.6% of pregnant women (555 out of 13,880) admitted to alcohol use and 1.4% (194 out of 13,880) admitted to binge drinking [1]. This survey also found that 15% of the women who were not pregnant admitted to binge drinking. This latter number is of concern because 50% of pregnancies are unplanned [2] and the average pregnancy is not recognized until 5 to 6 weeks after conception [3]. Therefore a woman who binge drinks could unknowingly expose the embryo to high blood alcohol concentrations. Even among the women who drink and believed they were not pregnant, a fraction are likely to have been in their early stages of pregnancy. Even low levels of prenatal alcohol (ethanol) exposure can produce birth defects termed fetal alcohol syndrome (FAS) [4–7] and /or the more encompassing fetal alcohol spectrum disorder (FASD). In addition to the craniofacial and neurological abnormalities commonly associated with FAS, up to 54% of live-born children with FAS present with cardiac anomalies [8], including valvuloseptal defects, pulmonary stenosis, Tetralogy of Fallot, and d-transposition of the great arteries [9]. Alcohol-induced congenital heart defects (CHDs) are frequently among the most life threatening CHDs and require surgical correction in the newborn and potentially intensive medical care throughout life. The estimated cost to society for the care of children and adults with FAS in the USA ranges from 1.4 billion to 9.7 billion dollars [10]. The mechanisms of these alcohol-induced CHDs remain largely unclear.

During development of avian and mammalian embryos, six major pairs of aortic arches (numbered I-VI) sequentially emerge. Cardiac neural crest cells (CNCCs) are a subset of neural crest cells (NCCs) that play a critical role in the development of the aortic arches [11]. These cells migrate dorsolaterally from the dorsal neural tube to the circumpharyngeal ridge and later progress into and populate the pharyngeal arches and a subset enter the cardiac outflow tract. These cells are critical for morphogenesis of the early aortic arches into the great vessels. Three of the original six pairs persist to form the brachiocephalic arteries (aortic arch III), the pulmonary arteries (aortic arch VI), and a segment of the aortic arch (aortic arch IV) [12, 13]. These remodeling events are very sensitive and vulnerable to perturbations that may result in congenital heart defects. The CNCCs in the pharyngeal arches develop into smooth muscle cells or other vascular support cells enveloping and supporting the persisting aortic arches [14, 15]. The absence or defects in, or the abnormal migration of CNCCs can result in an array of structural and functional defects of the great vessels and the heart, including misalignment of the great vessels, outflow tract septation defects (PTA), and abnormal myocardial function [16–20]. Ethanol exposure has been shown to disrupt NCCs in many ways [21–26].

Hemodynamic forces are known to play a significant role in the dynamic process of aortic arch formation and remodeling. Alterations to blood flow induced by mechanical manipulations such as aortic banding and vitelline vein clamping have been shown to result in congenital arterial defects such as coarctation of the aorta, interruption of the aortic arch, and double aortic arches [27–29]. In our previous studies using optical coherence tomography (OCT), we detected altered hemodynamic flow in early stage embryos by analyzing vitelline vessel blood flow [30, 31]. A refinement of this OCT technique allows the calculation of absolute blood flow [32]. We observed increased retrograde flow, abnormal pulsed Doppler trace morphology, and abnormal endocardial cushions volumes in our prenatal alcohol exposure model [31], where late stage vessel defects included missing or misaligned great vessels, and reduced great vessel diameters [33].

Previous studies documented normal aortic arch development through the use of corrosion casts, fluorescent dyes, and micro-particle imaging velocimetry (μPIV) [13, 34–36]. These investigators examined the structural remodeling of the vessels and measured the blood flow at various stages of development. The structural data has also been used to generate computational fluid dynamic modeling to quantify blood flow and shear stress during normal development. OCT has also been utilized to acquire structural data at specific stages of aortic

Biomedical Optics EXPRESS

arch formation. Here, we utilized OCT to image the blood flow and artery dimensions in the aortic arches of avian embryos. This allowed hemodynamic measurements without injection of exogenous factors into the blood or making assumptions required for computational fluid dynamics calculations. Hemodynamic measurements from control embryos were compared to ethanol-exposed embryos that develop CHDs.

OCT has been shown to be a very valuable tool for imaging cardiovascular embryonic development due to noninvasive depth resolved imaging, high spatial resolution (2-20 μm), and high temporal resolution (> 500 kHz line rates) [37–40]. OCT was first demonstrated to be useful for embryonic imaging of *Rana pipiens*, *Xenopus laevis*, and zebrafish [41]. It was soon afterwards shown to be capable of capturing both the structure and dynamics of the *Xenopus* embryonic heart [42]. Since these first studies, the development of many different animal models has been studied using OCT including mouse [43–47], *Xenopus* [48–51], *Drosophila* [52, 53], zebrafish [54, 55], quail [33, 56–59], and chicken [60–66]. Avian (quail/chicken) embryos have been a popular model for the study of cardiac development due to their easy accessibility for both visualization and manipulation. Yelbuz et al. utilized OCT to image the looping chick heart in excised samples and demonstrated the resulting 3-D visualizations enabled identifications of significant morphological differences between normal and abnormal embryos [60]. As OCT imaging speeds have increased, real-time imaging [62, 67, 68] and detailed 4-D acquisitions [45, 69–71] of the beating heart have been possible allowing for studies of the biomechanical forces at work during cardiovascular development [66, 72, 73].

In addition to structural imaging, OCT is capable of performing functional imaging to monitor and measuring moving reflectors in biological tissue by making use of the Doppler effect. Doppler OCT enables the measurement of absolute blood flow without injection of exogenous agents (fluorescent dyes) that might otherwise compromise the natural physiological hemodynamic forces. Many groups have utilized Doppler OCT to measure blood flow and hemodynamic forces under normal embryonic conditions [62, 74–77] and after various perturbation experiments [78–80]. Traditionally, to measure absolute blood flow with Doppler OCT, the angle between the imaging beam and the velocity vector of the flow (Doppler angle) needed to be determined. One method to determine this angle was by estimating the vessel orientation after acquiring a 3-D structural volume [81, 82]. However, the orientation of smaller more tortuous vessels can be difficult to determine and small errors in angle estimation can result in large errors in flow measurements [32]. An alternative method to determine the Doppler angle is by interrogating the same location at slightly different incident angles [83–88]. Unfortunately this technique requires significant increases to system and alignment complexity. Recently we have developed an easy to implement technique to acquire rapid absolute blood flow from individual B-scans [32]. This technique enables pulsatile flow measurements without the need for 3-D volumetric data or knowledge of blood vessel orientation.

Through the use of OCT we acquired structural and functional images of the aortic arches in both ethanol-exposed and control embryos. We previously established and studied a quail model of FAS that mimics a binge-drinking exposure at the stage of gastrulation, at which point a woman may not yet be aware of her pregnancy [31, 33]. This model was shown to result in abnormal development of the great arteries including defects such as double outlet right ventricle, misaligned aorta, and valve abnormalities that are similar to the cardiac defects observed in individuals with FAS [33]. It was our aim to longitudinally follow the progression of aortic arch remodeling from a stage when they have left-right symmetry to when they achieve their more mature asymmetric form to test the hypothesis that the final abnormal structure was preceded by altered shear stress in the relevant aortic arch. We also aimed to monitor neural crest cells that are critical for normal aortic arch morphogenesis by counting them as they migrated dorsolaterally away from the neural tube. Furthermore we measured the volume of (largely neural crest derived) mesenchyme surrounding the aortic

Biomedical Optics EXPRESS

arch arteries to determine whether reduction in the precursors of the support cells of the vessels (e.g., vascular smooth muscle cells) might be limiting the growth of the great vessel dimensions.

2. Experimental procedures

2.1 Embryo preparation

Fertilized quail eggs were incubated in a humidified incubator at 38°C until HH stage 4-5 (gastrulation). At this stage the embryo is highly vulnerable for the induction of CHDs [89]. The eggs were divided into 3 groups: ethanol treated group, vehicle control group and an untreated group. Ethanol treated eggs were injected with 40 µL of 50% ethanol in saline (approximately equivalent to a blood alcohol content of 0.179%), and vehicle control eggs were injected with 40 µL of saline. Ethanol dosage was based on previously published protocols [89] as being equivalent to one binge drinking episode in humans and reliably produced FAS-associated abnormal phenotypes. The solutions were injected into the air space at the blunt end of the egg and the eggs were then incubated until HH stage 14 where the eggshells were removed and the embryos were placed in petri dishes in the environmental OCT imaging chamber.

2.2 Optical coherence tomography imaging

Once in the Petri dish, the embryos were placed in an environmental OCT imaging chamber [90] with controlled temperature (38°C) and humidity to maintain near-physiological conditions. At HH stage 19 the aortic arches of the embryos were imaged with OCT. Stage 19 was selected for imaging because at this stage aortic arch III is well developed. This vessel develops into the brachiocephalic artery which was shown to have significantly reduced lumen area in our previous study of later-stage ethanol-exposed embryos. A frequency-domain OCT system with a quasi-telecentric scanner [91] was used to simultaneously collect structural and Doppler images. The OCT system utilizes a superluminescent diode centered at 1310nm with a FWHM of 75nm. A 1024-pixel InGaAs line-scan camera with a line rate of approximately 47 kHz was used to collect the interference fringes. The system has an axial and lateral resolution of ~10 µm in tissue.

2.3 Embryo staging

Typically, staging of embryos is performed by visualizing the embryo under a stereo microscope. Embryos are usually removed from the yolk due to the poor contrast. While this works well for individual terminal experiments it makes accurate staging during longitudinal experiments very challenging since the embryo must remain on the yolk for longer-term survival. Here, we verified embryonic developmental stages by 3-D OCT imaging. 3-D OCT data spanning an area of 4 mm by 4 mm were recorded in three acquisitions at sequential positions along the length of the embryo, with approximately 500 µm of overlap between each acquisition. These volumes were then processed and imported into Amira for visualization. Volume renderings were generated and *en face* images were generated. These 3 *en face* images were then stitched in Adobe Photoshop^{tm} CS3 to create a complete image of the entire embryo (Fig. 1(a)). This image rendering was used to verify developmental stages. Limb buds, wing buds, head size and body morphology were all examined and compared with known developmental stages [92, 93].

Biomedical Optics EXPRESS

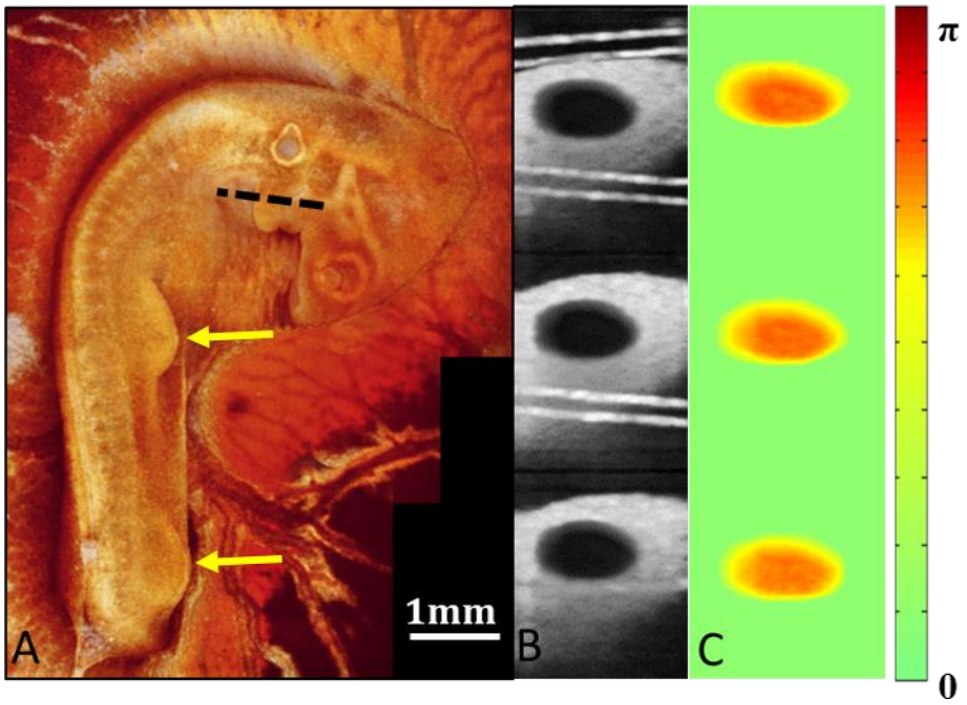

Fig. 1. Aortic arch imaging. (A) A projection of the 3-D volumetric OCT data acquired for embryonic developmental staging. The image clearly displays the limb buds and wing buds indicated by the yellow arrows. These limb buds along with general head and body morphology are necessary for accurate staging without removal of the embryo from the yolk. (B) A phase variance image was generated from the Doppler OCT data to segment the aortic arch vessel lumen. The cross-sectional OCT images used to generate the phase variance image were acquired at the pharyngeal arches indicated by the dotted line in A. (C) The segmentation was applied to the Doppler OCT images for absolute blood flow calculations.

2.4 Absolute blood flow calculation

OCT images of the pharyngeal arches were acquired at the location indicated by the dotted line in Fig. 1(a). In addition to structural images, Doppler OCT images were acquired from the aortic arches using dual beam delay encoded OCT as previously described [32] with a modification described below. This dual beam technique enabled absolute blood flow measurements without the need to acquire a 3-D volume. 214 B-scan images spanning 0.5mm were acquired over 4.6 seconds at one cross-sectional position. Structural and Doppler images were composed of 200 A-scans. Each A-scan in the Doppler image was generated from a five-line complex average. We coherently averaged the 214 B-scans to segment the lumen of the vessel as shown in Fig. 1(b). Blood flow in the lumen causes the OCT signal to decorrelate and diminishes the resulting averages. The segmentation was performed by simple thresholding and manual correction in Amira if necessary. The segmented Doppler images are displayed in Fig. 1(c). To obtain the instant flow, we modified our previous method using dual beam delay encoded OCT. Instead of solving the quadratic equation for the flow, we calculated the Doppler angle first, taking advantage of the assumption that the Doppler angle remains constant over the imaging session. By using all the B-scan frames, the Doppler angle can be determined with higher levels of confidence and the overall procedure is more robust. After we obtained the Doppler angle, flow can be calculated from any of the three images from each B-scan frame and the result can also be averaged to further reduce the noise. Results were analyzed for statistical significance using ANOVA.

Biomedical Optics EXPRESS

2.5 Hemodynamic measurements

Absolute blood flow was acquired at each time point of the heartbeat. The flow in the aortic arches can be modeled as a tube in which the flow is laminar and all points are moving in the same direction. The shear stress can then be calculated using the relationship:

$$\tau_{\omega} = \frac{4Q\mu}{\pi r^3} \quad (1)$$

where τ_{ω} is the wall shear stress, Q is flow, r is the vessel radius, and μ is the fluid viscosity. We assumed a fluid viscosity of 5 mPa based on previous literature [34, 94]. The average absolute blood flow and shear stress was calculated over a heart cycle. The peak forward and peak retrograde shear stress for a data set was defined as the 95th and the 5th percentile value respectively. The oscillatory shear index (OSI) was also determined over the duration of a heartbeat as detailed in [95]. The OSI ranges from 0, when the shear is always in the forward direction, to 0.5 when the average shear stress over time is zero. Data for all hemodynamic measurements were analyzed for statistical significance using ANOVA analysis.

2.6 Pharyngeal arch tissue measurement

3-D OCT volumes of the pharyngeal arches were acquired from uninjected, saline, and ethanol-exposed embryos. The volumes imaged covered a region of 1mm x 2mm and 9 images were acquired at each imaging location for averaging. This area includes the connection from the heart tube as well as the connection to the dorsal aorta and reflects the mesenchymal tissue volume comprised primarily of cardiac neural crest-derived cells. The averaged structural images were imported into Amira for 3-D visualization and segmentation. A cross sectional plane orthogonal to the vessel direction was manually selected at the midpoint of the aortic arch from the averaged 3-D volume. This slice was then manually segmented to measure the lumen area and the area of the surrounding mesenchymal tissue of the aortic arch. Both the lumen and tissue area measurements were analyzed for statistical significance using an ANOVA analysis.

2.7 Neural crest cell immuno-labeling

Three uninjected embryos and three ethanol-exposed embryos were collected at HH Stage 13 when the cardiac neural crest cells have migrated ventrolaterally away from the neural tube and are approaching or have reached the circumpharyngeal ridge. Embryos were fixed in 4% PFA, washed in PBS and incubated in sucrose overnight for cryopreservation prior to freezing. They were then cryosectioned (10μm thick) transversely and double stained for HNK-1 and AP-2, markers for migrating neural crest cells. Sections from approximately the same transverse level for each embryo were immunostained and images were recorded where the neural crest cells enter the circumpharyngeal ridge. A region of interest (ROI) was chosen as the site populated by neural crest cells in uninjected embryos and delineated within the image. This ROI was chosen as consistently as possible in each embryo sample. In this ROI, the ratio of the number of HNK-1 and AP-2 positive cells to the total number of cells (with DAPI-stained nuclei) was obtained by cell counting for each embryo on both the left and right sides. Results were analyzed for statistical significance using the chi-square test.

3. Results

Pulsed Doppler traces were acquired from the right 3rd aortic arch of ethanol-exposed, saline-injected, and uninjected cohorts of embryos at HH stage 19 of development. Ethanol-exposed embryos were observed to have significantly increased retrograde blood flow compared to saline-injected and uninjected control embryos. The average percentage of retrograde blood flow for ethanol-exposed embryos was 8.2% while the uninjected and saline-injected embryos were observed to have averages of 3.5% and 3.1%, respectively. Ethanol-exposed embryos

Biomedical Optics EXPRESS

were also observed to have altered pulsed Doppler trace morphology. The control and saline-injected embryos possessed a positive peak with a prominent shoulder and a negative peak. The pulsed Doppler waveforms for the ethanol-exposed embryos often lacked a distinct shoulder (Fig. 2(b)). These alterations to retrograde blood flow and pulsed Doppler waveform morphology are consistent with those shown previously at the vitelline artery of stage 19 embryos [31], the same stage as observed in this study.

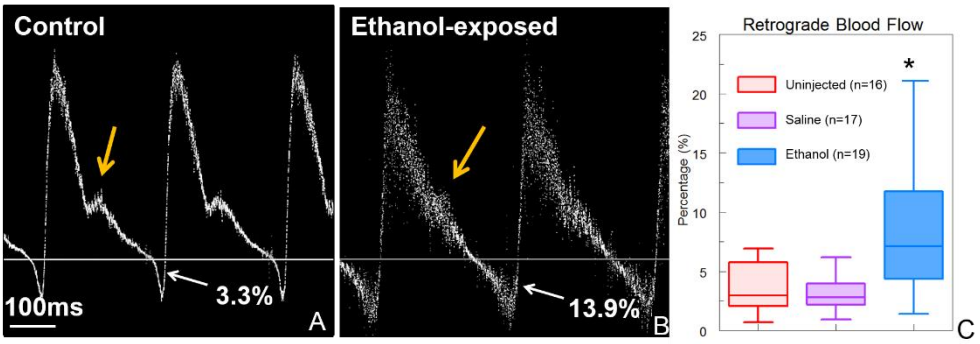

Fig. 2. Pulsed Doppler traces were acquired in the 3rd aortic arch of control (uninjected) and ethanol exposed HH stage 19 embryos. (A) Both uninjected (n = 16) and saline (n = 17) embryos had pulsed Doppler traces with a positive peak and a prominent shoulder (orange arrow) followed by a minor negative peak indicating retrograde blood flow. (B) Pulsed Doppler traces from ethanol-exposed embryos (n = 19) showed increased retrograde blood flow and were often missing a shoulder (orange arrow). (C) Ethanol-exposed embryos exhibited a significant increase in average percentage of retrograde blood flow compared with saline or uninjected embryos. * indicates $p<0.05$

Cohorts of ethanol-exposed, saline-injected, and uninjected embryos were imaged using Doppler OCT at HH stage 19 of development in the aortic arch region. The average blood flow was determined over a heartbeat from dual beam delay encoded images as previously described [32] with a modification described above. Ethanol-exposed embryos were observed to have significantly higher average blood flow compared to saline and uninjected control embryos (Fig. 3(a)). The average blood flow in the ethanol-exposed embryos was 0.26 μL/sec compared with the uninjected and saline embryos having 0.15 μL/sec and 0.14 μL/sec, respectively. The shear stress produced by the blood was also calculated. Due to the fact that the vessels cross sectional areas were the same while the blood flow was increased, the shear stress in ethanol-exposed embryos were significantly higher (Fig. 3(b)). Ethanol exposed embryos had an average shear stress of 0.52 Pa compared with uninjected embryos with 0.27 Pa and saline injected embryos with 0.29 Pa. To calculate the average shear stress over the duration of a heartbeat, the shear stress at each time point was calculated. The temporally resolved shear stress enabled the measurement of the oscillatory shear index (OSI) for each embryo. Due to the increase in retrograde blood flow, the ethanol-exposed embryos exhibited a higher OSI (0.08) than the uninjected (0.05) or saline injected (0.05) embryos (Fig. 3(c)).

It has been shown using the zebrafish model that oscillating blood flow is an important factor in cardiovascular development [96, 97]. The results of this study suggested that the peak forward and reverse blood shear stress, rather than the average blood flow, may be a critical factor involved in the hemodynamic response to ethanol exposure. To explore this possibility, we determined the peak magnitude of shear stress produced by both forward blood flow as well as retrograde blood flow. The ethanol-exposed embryos exhibited significantly higher magnitudes of shear stress in both the forward and retrograde direction compared with the control and saline-injected embryos (Fig. 3(d) and 3(e)). On average, ethanol exposed embryos had a peak shear stress of 1.81 Pa in the forward direction and 0.43 Pa in the retrograde direction. Uninjected embryos had an average forward shear stress of

Biomedical Optics EXPRESS

0.87 Pa and a retrograde shear stress of 0.15 Pa, while saline-injected embryos had an average forward shear stress of 0.98 Pa and a retrograde shear stress of 0.18 Pa.

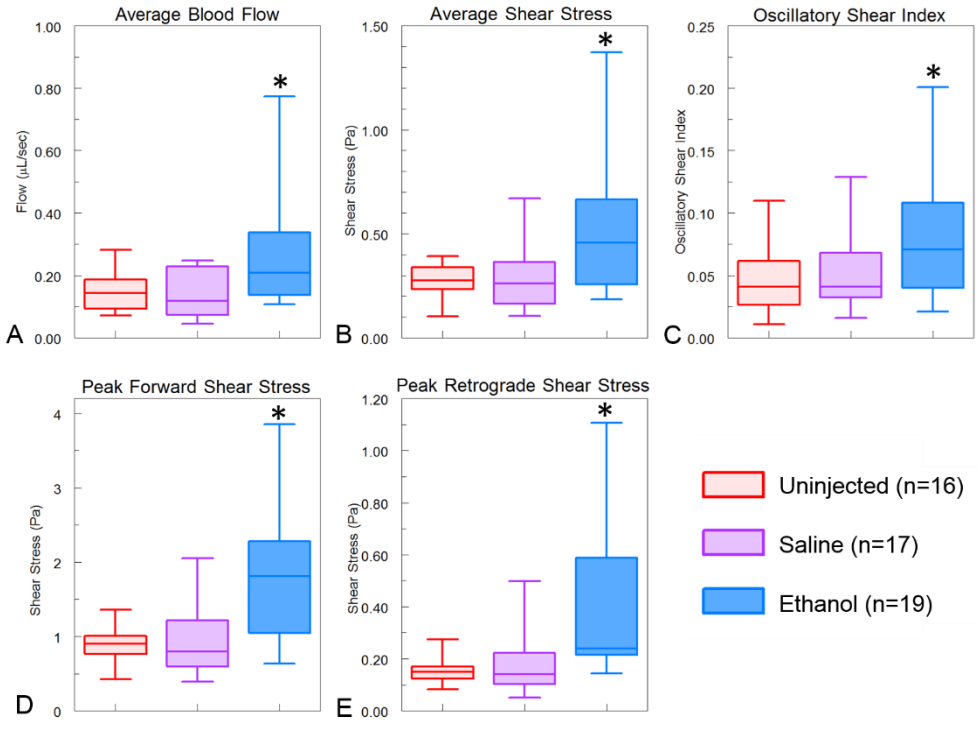

Fig. 3. Hemodynamic measurements. Ethanol-exposed embryos exhibited higher levels of all hemodynamic measurements. (A) Average blood flow over a heartbeat from multiple B-scan images. (B) These same images were used to determine the average shear stress. Ethanol-exposed embryos had significantly higher average blood flow and shear stress. (C) The shear stress values over the heartbeat were used to determine the oscillatory shear index which was higher in ethanol-exposed embryos due to the higher retrograde blood flow. (D and E) the peak forward and retrograde shear stress were determined and shown to be higher in ethanol-exposed embryos in comparison with uninjected and saline controls. *indicates $p < 0.05$.

In addition to the hemodynamic alterations, we determined whether there were any changes to the morphology of the aortic arch vessel or the overall pharyngeal arch (which includes both the mesenchyme and the blood vessel). Neural crest derivatives are known to be a major contributor to the aortic arch mesenchyme [14, 98–102] and previous studies support that NCCs were affected by ethanol exposure (reviewed in [103]). An orthogonal slice from the 3-D structural volume of the aortic arches was selected and segmented to measure the cross sectional areas of the aortic arch artery lumen and the surrounding tissue (Fig. 4(a), 4(b)). There was no difference in the vessel lumen cross sectional area in any of the cohorts of embryos (Fig. 4(c)). The average lumen area for the uninjected, saline-injected, and ethanol-exposed embryos was 0.034 mm^2, 0.033 mm^2, and 0.034 mm^2, respectively (Fig. 4(c)). In contrast, the ethanol-exposed embryos had significantly smaller mesenchymal tissue areas surrounding the aortic arch vessels with an average of 0.055 mm^2. Uninjected embryos and saline-injected embryos had similar cross sectional areas of tissue with an average of 0.063 mm^2 and 0.065 mm^2, respectively (Fig. 4(d)).

Biomedical Optics EXPRESS

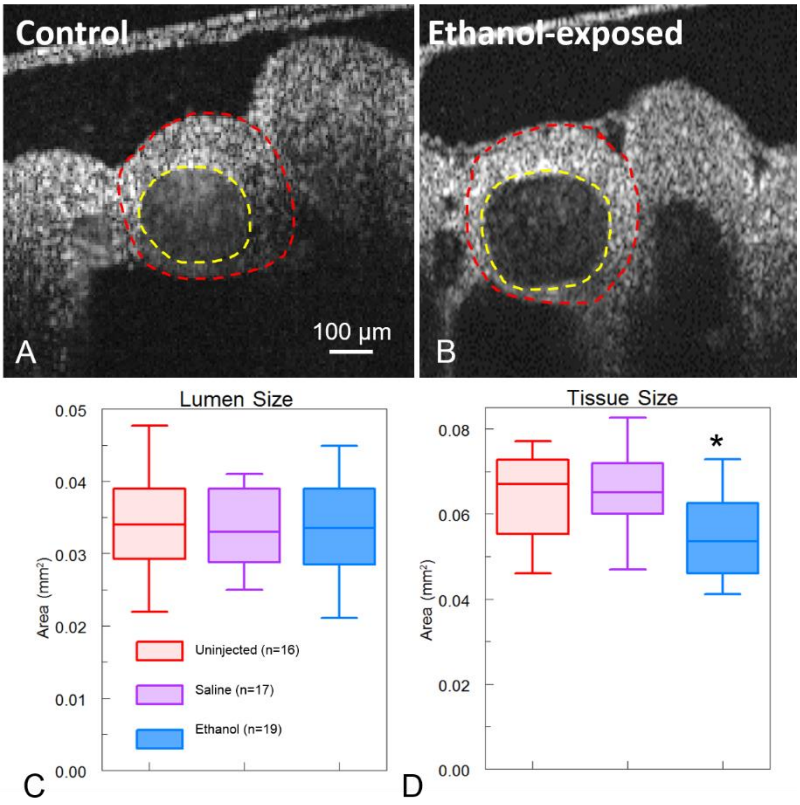

Fig. 4. Pharyngeal arch mesenchymal tissue measurements. An orthogonal slice from a 3-D volumetric acquisition of the 3rd aortic arch of an uninjected (A) and ethanol-exposed (B) embryo. The lumen area was segmented as indicated by the yellow dotted line. The surrounding pharyngeal arch tissue was then segmented as indicated by the red dotted line. (C) Ethanol-exposed embryos (n = 19) did not have a statistically significant difference in the lumen cross sectional area compared with uninjected (n = 16) and saline (n = 17) embryos. (D) The surrounding pharyngeal arch tissue cross sectional area was statistically smaller in ethanol exposed embryos in comparison to uninjected and saline embryos. * indicates $p<0.05$.

Because the area of the aortic arch mesenchyme (which is largely derived from neural crest cells) was significantly smaller due to ethanol exposure, we investigated cardiac neural crest development at an earlier stage (HH stage 13) when these cells are still actively migrating and have reached the circumpharyngeal ridge. At this point in development they are positive for two markers of neural crest, HNK-1 and AP-2. Antibodies for both markers were utilized to produce stronger stationing. The percentage of migrating neural crest cells in an area of the circumpharyngeal ridge was obtained by calculating the ratio of HNK-1 and AP-2 positive cells to the total number of cells as detected by DAPI positive nuclei in that area. Analysis of control and ethanol-exposed embryos revealed that due to ethanol exposure, there was a 27% decrease in migrating neural crest cells on the left side of the embryo and a 45% decrease in migrating neural crest cells on the right side of the embryo ($p<0.001$) (Fig. 5). These findings suggest that neural crest development is abnormal even at these earlier stages possibly due to ethanol-induced anomalies in neural crest induction, proliferation and/or migration.

Biomedical Optics EXPRESS

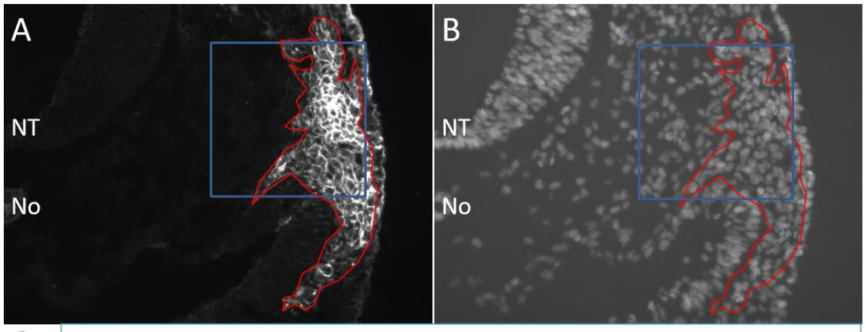

C

Percentage of Migrating NCCs at the Beginning of the Circumpharyngeal Ridge in HH Stage 13 Embryos

	Left Side	Right Side
Control (n=3)	50%	51%
Ethanol (n=3)	37%	28%

Fig. 5. Quantification of cardiac neural crest mid-migration. Transverse cryosections of stage 13 embryos at the level of the cardiac neural crest were immunofluorescently stained using HNK-1 and anti-AP-2 antibodies to identify neural crest cells (A). Cyrosections were also co-stained with DAPI to identify all cell nuclei (B) for quantification. The area of HNK-1/AP-2 positive neural crest cells are outlined in red (A,B) with the area that was selected for quantification outlined in blue regions of interest (A,B). The area selected is within the beginning of the circumpharyngeal ridge. Both the left and right sides of the embryo were similarly imaged for quantification. NT = neural tube; No = notochord.

4. Discussion

In this study, we used OCT to image the structure and function of the aortic arches of cohorts of HH stage 19 embryos. The embryos were divided into three groups consisting of uninjected, saline-injected, and ethanol-exposed embryos. OCT images were used to acquire hemodynamic measurements including percentage of retrograde blood flow, average blood flow, average shear stress, oscillatory shear index, peak forward and peak retrograde shear stress. These measurements were possible due to a recently-developed orientation-independent, dual-angle Doppler OCT technique which enabled rapid measurement of absolute blood flow in a region where vessel orientation is challenging to determine due to large curvatures [32]. Each hemodynamic measurement was found to be significantly higher in ethanol-exposed embryos compared with those obtained from both uninjected and saline-control embryos.

To study the neural crest cell derivatives, the size of the aortic arches was measured using structural OCT volumes and the number of neural crest derivatives migrating to the aortic arches during an earlier stage was quantified. The aortic arch artery lumen cross sectional area was found to be similar across all cohorts of embryos while the area of the mesenchymal tissue surrounding the vessel was significantly smaller in ethanol-exposed embryos compared with the controls. The mesenchyme within the pharyngeal arches is known to have a substantial contribution from neural crest derived cells [14, 98, 100–102]. There were also fewer neural crest cells migrating dorsolaterally, perhaps due to abnormal migration patterns, reduced proliferation, or simply increased cell death anywhere along their developmental program. The left-right asymmetry of the number of neural crest cells that were detected before ethanol treatment and found to be higher after ethanol treatment was unexpected and intriguing. In zebrafish, left-right asymmetry of a genetically labeled sub-set of migratory neural crest cell derivatives in the head region was enhanced by ethanol exposure. The migration of these cells was reduced and disorganized compared to that of control embryos [104]. This disrupted the nearly mirror image migration patterns of NCCs observed in control

Biomedical Optics EXPRESS

embryos. The authors hypothesized that this exaggerated left-right asymmetry may explain the higher incidence of left-right facial asymmetries detected in individuals with FAS [105]. A similar effect on immediately adjacent cardiac neural crest cell migration in avian embryos in our PAE model could explain the lower cardiac neural crest derived cell numbers at the circumpharyngeal ridge and the smaller pharyngeal mesenchyme.

Smaller pharyngeal tissue size in ethanol-exposed embryos may be the result of abnormal CNCC development. Abnormal NCC development may also play a role in the observed hemodynamic changes in ethanol exposed embryos. Targeted ablation of the cardiac NCCs has been shown to contribute to altered hemodynamic parameters, such as blood flow velocity, wall stress, cardiac output, etc [106–109]. Interestingly, cardiac function was altered at stages well before CNCCs are known to enter the heart. Depressed calcium transients in the myocardium were detected as early as stage 14, 24 h after CNCC ablation and 48 h before NCCs enter the outflow tract of the heart in chicken embryos [110, 111]. Subsequent studies have pointed to an indirect effect of CNCCs on the differentiating secondary heart field that may have altered cardiac function via abnormal FGF signaling [11]. The altered hemodynamic forces measured here are likely a result of the combination of CNCCs related morphological and functional changes due to ethanol exposure. The smaller amount of mesenchymal tissue around each aortic arch artery may alter their ability to remodel and be enveloped by smooth muscle cells. This could eventually impede vessel growth and result in reduced great vessel diameters that we observed at later stages (post-septation) in this model of PAE [33].

We previously reported higher retrograde blood flow and abnormal pulsed Doppler trace morphology in ethanol-exposed embryos [31]. Those measurements were taken in the left vitelline arteries of HH stage 19 embryos. We reported ethanol-exposed embryos of the same stage to have 10.96% of retrograde blood flow, uninjected embryos to have 2.42% of retrograde blood flow, and saline-injected controls to have 3.34% of retrograde blood flow. These numbers are in close agreement with those presented here captured at the aortic arch 3 and the small discrepancies are likely due to the fact that the pulsed Doppler trace was acquired in a different location further away from the heart. Many of the traces acquired from the aortic arch of the ethanol-exposed embryos exhibited a slightly more noisy trace compared to traces obtained from other vessel positions [31]. This is due to the curved body phenotype typically exhibited by ethanol-exposed embryos [31] causing the aortic arches to be located in a less accessible location. This change in location results in a lower signal to noise ratio in the OCT images resulting in a more blurred trace. Despite this, the overall shape of the trace still clearly shows the altered hemodynamics exhibited by the ethanol-exposed embryos. Pulsed Doppler traces recorded at the aortic arches should more accurately reflect cardiac function considering that they are the first vessels that the blood enters upon exiting the heart. Both the previously reported pulsed Doppler traces as well as those presented here showed abnormal trace morphology in ethanol-exposed embryos, a reduced or missing shoulder. The detection of this abnormality at a site immediately beyond the heart tube supports that this reduced or absent shoulder is the result of abnormal atrioventricular cardiac cushion formation induced by ethanol exposure [31,112].

Funding

National Institutes of Health (RO1HL083048, R01HL095717, R21-HL115373, R01HL126747); American Heart Association postdoctoral fellowship to GK (14POST19960016); Interdisciplinary Biomedical Imaging Training Program NIH (T32EB007509).